Sustainable Energy & Fuels

Accepted Manuscript

This article can be cited before page numbers have been issued, to do this please use: K. K. Karuppanan, A. V. Raghu, M. K. Panthalingal, V. Thiruvenkatam, K. Palanisamy and B. Pullithadathil, *Sustainable Energy Fuels*, 2019, DOI: 10.1039/C8SE00552D.

ROYAL SOCIETY OF CHEMISTRY

rsc.li/sustainable-energy

View Article Online
DOI: 10.1039/C8SE00552D

Journal Name

ARTICLE

3D-Porous Electrocatalytic Foam Based on Pt@N-Doped Graphene for High Performance and Durable Polymer Electrolyte Membrane Fuel Cells.

Received 00th January 20xx,
Accepted 00th January 20xx

DOI: 10.1039/x0xx00000x

www.rsc.org/

Karthikeyan K Karuppanan,[a] Appu V Raghu,[a] Manoj Kumar Panthalingal,[b] Vijayaraghavan Thiruvenkatam,[a] Karthikeyan P[c] and Biji Pullithadathil*[a,d]

A 3D porous nitrogen-doped graphene foam with uniformly grafted platinum electrocatalyst (2-3 nm) (3D-Pt@N-Graphene foam) has been developed using simple hydrothermal synthesis for high performance proton exchange membrane (PEM) fuel cells. Excellent electrocatalytic activity towards ORR in acidic medium has been exhibited by Pt@N-Graphene foam with a favorable 4-electron transfer pathway resulting in the augmentation of active triple phase boundary sites. A positive shift of onset potential (989 mV) and half wave potential (895 mV) with a high limiting current density of 4.675 mA/cm^2 exhibited by 3D-Pt@N-Graphene foam was found to be comparatively greater than that of Pt/C catalyst with high durability. Presence of pyridinic-N and pyrrolic-N species in the highly compressible 3D-Pt@N-Graphene foam contributed to the enhancement of electrocatalytic activity, while graphitic-N improved the electrical conductivity of the material facilitating the electron transport during ORR process. Compared to commercial Pt/C electrocatalyst, 3D-Pt@N-graphene foam based on membrane electrode assembly exhibited four times higher power density (394 mW/cm^2) and current density (1036 mA/cm^2) owing to the favorable mass transport due to the hierarchical porous network, high specific surface area, nitrogen doping, uniform distribution of Pt nanoparticles and abundant active sites on the support material. The material demonstrates a new rational design for the fabrication of highly efficient electrocatalyst assembly for flexible PEMFCs.

Introduction

The imminent and rising global energy demand and the depletion of fossil fuels have promoted the research on the development of sustainable and clean energy resources. Polymer exchange membrane fuelcells (PEMFCs) are regarded as a potential device for transport and mobile applications, owing to their advantages such as, zero emission, high power density, minimal corrosion problems, low operating temperature, and fast startup[1–5]. However, performance of cathodic side of the fuel cell is still remaining as a big challenge due to the sluggish reaction kinetics of oxygen reduction. Until now, platinum and its alloys have been widely used as a benchmark electrocatalyst materials in PEMFCs owing to its advantages such as favorable output voltage, relatively low electrochemical over potential, reactivity at low temperature and easy bonding with hydrogen and oxygen to form final products[6–10]. The showstopper of the platinum electrocatalyst towards the widespread commercial success of fuelcells is high cost, limited abundance, sluggish electron transfer kinetics and inadequate durability. In order to overcome these primary obstacles for large-scale commercialization, a viable approach should be employed for developing active electrocatalysts with minimum loading and maximum utilization. It is well known that the performance of the fuelcell greatly depends on the size, shape and distribution of catalyst nanoparticles on the support materials [6,11,12]. In addition to this, catalyst support materials pose strong impact on controlling the properties, such as high specific surface area, superior electrical conductivity for rapid electron transfer during the reactions, good electrochemical stability under harsh operating conditions and strong immobilization of the catalyst in order to improvise the triple phase boundaries in the fuel cell electrodes[13]. Pt supported on carbon black (Pt/C) is most widely used as the electrocatalyst for cathodic reaction[14–17]. However, the performance of the fuelcell is degraded due to the electrochemical oxidation of the support material resulting in detachment of the catalyst and simultaneous agglomeration which limit their practical applications[11,18–21]. In order to improve the activity and minimize the platinum loading, the electrocatalyst must be anchored on a suitable support material having high specific

[a] Nanosensor Laboratory, PSG Institute of Advanced Studies, Coimbatore-641004, INDIA.
[b] Department of Mechanical Engineering, PSG Institute of Technology and Applied Research, Coimbatore- 641 062, INDIA.
[c] Department of Automobile Engineering, PSG College of Technology, Coimbatore-641004, INDIA.
[d] Department of Chemistry, PSG College of Technology, Coimbathore-641004, INDIA

* Corresponding author E-mail: bijuja123@yahoo.co.in

Electronic Supplementary Information (ESI) available: Few detailed information are provided in supporting information, including synthetic strategy, UV-Vis, XRD, Raman, FTIR, TG, XPS, TEM, AFM, SEM, BET, electrochemical characterizations and comparison of the ORR results of the prepared samples. [See DOI: 10.1039/x0xx00000x

surface area, good electrical conductivity, low cost and less corrosion issues.

In recent decades, two-dimensional (2D) layered nanomaterials, such as graphene have been recognized as unique carbon materials and those are increasingly important for fuelcell applications due to their fascinating properties, such as high mechanical and chemical stability, large thermal conductivity, high specific surface area and excellent electronic conductivity by raising the Fermi level to the conduction band[22–25]. In recent years, investigation of doping of heteroatoms in graphene structure for ORR is becoming an important topic in the field of fuelcells [26,27]. Introduction of heteroatoms such as nitrogen in graphene lattice can facilitate i) faster nucleation and growth kinetics of the catalyst leading to small size and uniform dispersion, ii) increased chemical affinity between catalyst and support which results enhanced stability and iii) enhanced electronic conductivity due to the modification in electronic structure[4,28]. Untill now, nitrogen has been realized as an ideal dopant for graphene among other dopants owing to their high electronegativity and comparable atomic size to carbon[29,30]. Very recently, several reports suggested the use of nitrogen-doped graphene as a highly efficient and stable metal-free electrocatalyst for ORR[28,31–34], representing a breakthrough for N-containing electrocatalyst for application in PEM fuelcells. Unlike graphene, nitrogen-doped graphene exhibit high electron density and electron donating properties which can change the valence band structure, including the raising of density of π states near to the Fermi level leading to reduction of work function[35]. Although higher nitrogen content in graphene structure could create active sites, poor electron transfer hampers its activity[35]. Tremendous efforts have been made in the last few years to interpret the active sites and catalytic mechanism in nitrogen-doped graphene towards oxygen reduction reaction, but there are studies still under debate. Meanwhile, the two-dimensional structure of graphene sheets was tending to be irreversibly agglomerated by Van der Waals force and π-π stacking interactions during fabrication which reduces the mass transport phenomenon in electrode materials[23,36,37]. Recent studies demonstrated the integration of 2D graphene layers into three-dimensional porous structure for a broad range applications due to their large surface area and high porosity[38–44]. Although graphene and nitrogen-doped counterparts have been synthesized and studied for ORR, three-dimensional hierarchical, porous structures of these materials with large specific surface area, unique porous architecture, high doping level of heteroatoms, high mechanical stability and multidimensional electrical conduction pathways have potential capabilities for improving the triple phase boundaries and designing of high performance fuel cells electrodes.

In this scenario, we have made an attempt to investigate the synergistic effect of nitrogen-doped graphene-based 3D-foam integrated with platinum electrocatalyst for achieving high performance in PEMFCs. A facile synthesis of nitrogen-doped graphene foam from the reducing agents of urea, hydrazine hydrate, ammonia was used to fabricate 3D hierarchical porous support material for Pt electrocatalyst for efficient ORR. Unique structural, morphological and compositional features of 3D-Pt@N-Graphene foam exhibited excellent electrical conductivity, high onset potential, half-wave potential and long-term stability in oxygen reduction reactions in acidic medium. The augmentation in fuel cell performance is mainly attributed to the feasible mass transfer, hierarchical porous structure with high specific surface area, optimal level of nitrogen doping and homogeneous dispersion of Pt nanoparticles. The faster reaction kinetics, high durability of 3D-Pt@N-doped garaphene foam surpasses the performance of state-of-the-art commercial Pt/C electrocatalyst.

Experimental Section

Materials and Methods

Natural graphite flakes (< 20 μm flakes, Sigma-Aldrich,), potassium permanganate ($KMnO_4$), phosphoric acid (85 % H_3PO_4), sulphuric acid (98 % H_2SO_4), hydrogen peroxide(30 % H_2O_2), hydrochloric acid (HCl) hexachloroplatinic acid (H_2PtCl_6·6H2O, Sigma-Aldrich), ethylene glycol (EG) and sodium hydroxide (NaOH) were used for the synthesis of Pt@N-Graphene.Pt/C (20%, Vulcan XC-72), Nafion solution and membranes (Dupont) and polytetrafluoroethylene (PTFE) (60%, Aldrich) were purchased. Commercially available polyurethane sponge was purchased and used for fabrication of 3D-Pt@N-Graphene foam. All reagents were of analytical grade and directly used without any further purification.

Preparation of Graphene

In the first step, an improved Hummer's method was used to prepare exfoliated graphene oxide from an oxidation of natural graphite flake powder[45]. The detailed experimental procedure is explained as follows. In a typical synthesis, graphite flakes (3g) were dispersed into the mixture of 500 ml H_3PO_4/H_2SO_4 (1:9 ratio) under constant stirring for 1 h, then potassium permanganate (18.0 g) was added slowly in a sequence. The solution was kept at 50 °C and stirred for 12 h. The reaction mixture was cooled to room temperature and poured onto ice (400 ml) containing 3 ml of 30 % H_2O_2. Then the reaction product was collected and filtered through a metal U.S standard testing sieve (pore size ~300 μm) and further filtered through a polyester fiber while the supernatant liquid was decanted away. The remaining solution was washed successively with water (200 ml), 30 % HCl (200 ml) and ethanol (200 ml). Then, the mixture was washed thrice with water by centrifugation (4000 rpm for 4 h) and the supernatant was decanted away. After that, the resultant material was coagulated with ether and filtered through a PTFE membrane (pore size ~0.45 μm). Finally, the obtained solid material was dried in a vacuum at room temperature for 12 h. The as-synthesized dispersion of GO in water displayed dark yellow colour, indicating a successful oxidation of graphite to GO. In the second step, further chemical reduction of graphene oxide was carried out using hydrazine hydrate (N_2H_4) to achieve graphene[46].

Preparation of 3D N-graphene Foam

The fabrication procedure of 3D porous N-graphene foam through one-pot hydrothermal method is illustrated in Figure S1. Initially, the graphene sheets were dispersed in aqueous

View Article Online
DOI: 10.1039/C8SE00552D

solution containing urea, hydrazine hydrate and ammonia as a reducing agent. A 25 ml of 1.5 mg/mL graphene aqueous dispersion with a given amount of urea, hydrazine hydrate and ammonia was ultrasonicated for 1 h. Then the commercial porous PU sponge template was completely immersed in the solution, ultrasonicated for about 1 h and squeezed several times, so that the graphene layers would crosslink with skeletons of PU. Then, it is sealed in a 50 mL Teflon-lined autoclave and maintained at 90 °C for 3 h, leading to the encapsulation of nitrogen-doped graphene sheets around the skeletons of PU sponge. The autoclave was cooled to room temperature and the collected samples were washed with de-ionized water to remove the residual of dopant chemicals. At last, the resultant samples were dried in a vacuum oven at 80 °C for 24 h. Finally, the N-graphene with high content of nitrogen encapsulated on PU foam was pyrolyzed at 500 °C for 1 hr under argon atmosphere. The synthetic procedure of free-standing 3D-Pt@N-Graphene foam is depicted in Figure 1.

Preparation of 3D-Pt@N-Graphene

The synthesis scheme of 3D-Pt@N-graphene foam is illustrated in Figure 1. The Pt nanoparticles were incorporated on N-graphene foam by using hydrothermal polyol-reduction method[47]. To achieve that, N-graphene foam (60 mg) was soaked in a mixture of ethylene glycol (20 ml) for 1h and a calculated amount of $H_2PtCl_6.6H_2O$ was added slowly. Then the pH was adjusted to 11 by adding NaOH (2.5 M). The suspension was transferred into 50 mL Teflon-lined autoclave and heated at 120 °C for 4 h. Finally, the 3D-Pt@N-Graphene foam was washed with de-ionized water and then obtained product was dried in vacuum oven at 80 °C for 12 h. The final product was labelled as 3D-Pt@N-Graphene foam. Pt@N-Graphene also was prepared using the same synthesis method for a comparison purpose. The Pt content in the various electrocatalyst was determined by inductively coupled plasma atomic emission spectroscopy (ICP-AES) and Pt loading for the 3D-Pt@N-Graphene foam, Pt@N-Graphene and Pt/C were estimated to be 19.48 wt%, 19.22 wt% and 19.87 wt%, respectively.

Fabrication of MEA and single cell testing

In order to explore the promising application of electrocatalyst in acid fuelcell, membrane electrode assembly (MEA) with an active area of 5x5 cm^2 was fabricated by hot bonded (10 MPa at 130 °C for 2 mins) with a pretreated Nafion® 117 membrane (Dupont). Firstly, the electrocatalyst slurry of 20 % electrocatalyst, such as Pt@N-Graphene and Pt/C was prepared by ultrasonication with the mixture of isopropanol, 5 wt. % Nafion ionomer solution (DuPont) and ultrapure water for 1 hour. Then, the resulting slurry was sprayed coated on the one side of the Teflon treated carbon paper (Toray) to form a cathode catalyst layer. Similarly, commercial Pt/C (Vulcan XC-72) was also coated using the same method to form an anode. The catalyst loadings on the cathode side were 0.3 mg/cm^2 and Pt loadings on the anodes were 0.1 mg cm^2, respectively. Then, the assembled single fuel cell with the as-prepared MEAs was tested using fuel cell test station (Biologic FCT-50S). The humidifying temperature of hydrogen and oxygen was maintained at 40°C and the flow rate of the hydrogen and oxygen gases was 400 and 200 ml/min, respectively.

Characterization Techniques

Structural characterization of the synthesized samples was investigated by recording X-ray diffraction (XRD) patterns on a powder X-ray diffractometer (Panalytical X-pert) equipped with Cu-Kα radiation (λ=1.5406 Å) as source. The Patterns were recorded between 5° and 90° 2θ with a working voltage and current was 40 kV and 30 mA, respectively. The microstructural parameters were determined using JCPDS software. Raman spectroscopy analysis was performed using Ar ion laser with an excitation wavelength of (514.5 nm). The attenuated total reflectance Fourier-transform infrared (ATR-FTIR) analysis was carried out on a IR Affinity series 1S (Shimadzu, Japan) in the spectral ranges from 4500 to 400 cm^{-1} with a resolution of 2 cm^{-1} to elucidate the functional group of synthesized materials. The samples were mixed with potassium bromide (KBr, Sigma-Aldrich) by grinding before being pressed into pellets. Thermogravimetry (DSC/TG) analysis was performed using NETZSCH (Jupiter STA449F3), Germany. The morphology, size, distribution and microstructure of the prepared materials were characterized by high-resolution transmission electron microscopy (HRTEM, JEOL JEM 2100, Japan) with an accelerating voltage of 200 kV, scanning electron microscopy (SEM, Carl Zeiss) with an accelerating voltage of 20 Kv. Atomic force microscopy (AFM) measurement was performed on NTMDT (NTEGRA prima, Russia) semi-contact mode operation using silicon catilevers (spring constant ~0.3-6.6 Nm^{-1}, resonance frequency ~97.0 kHz).The chemical composition of the samples was analyzed by X-ray photoelectron spectroscopy (XPS) using a Thermoscientific instrument equipped with Al Kα (hυ = 1486.6 eV) achromatic radiation source. Elemental chemical ratios of the samples were calculated from the areas of XPS peaks. The nitrogen physisorption isotherms were measured at 77 K using an Autosorb-1apparatus (Quantachrome, Florida, USA) after degassing at 200 °C and the corresponding surface areas were determined based on the Brunauer-Emmett-Teller (BET) equation. The pore size distributions were calculated by the nonlocal density functional theory (NLDFT) method. The mechanical properties of the graphene foams were analyzed via compression tests using an MARK-10 corporation, Force Gauge model M5-20 (USA). The specimens were cut into blocks with dimensions of 1×1×8 mm^3 were compressed at various strains levels of 20-80 % with a crosshead speed of 30 mm/min. In order to illustrate the wettability features, the water contact angle measurements was conducted on a Dataphysics instrument (OCA 15, Germany) using a water drop (V = 10 µL) gently placed on the surface of the sample.

Electrochemical measurements

The ORR performance and stability of the samples were studied using a CHI600E electrochemical workstation (CH Instruments, Inc. USA). The standard three-electrode system was used, where glassy carbon electrodes (GC), platinum wire, and Ag/AgCl electrode were served as a working, counter and reference electrodes, respectively. All potentials were

converted to a RHE scale. The ORR activity and four electron selectivity of the 3D-Pt@N-Graphene sample were evaluated using rotating disk electrode (RDE) experiments. This RD electrode consisted of a glassy carbon disc (geometric area: 0.0314 cm^2) and linear sweep voltammetry experiments were conducted at various rotation rates. The preparation of working electrodes is as follows: The working electrode was mechanically polished with 0.3 and 0.05 µm alumina slurry to obtain a mirror-like surface and then washed with Mill-Q water and acetone. 1 mg of the prepared electrocatalyst was dissolved in 1 mL solvent mixture of Nafion and water (v/v ratio=1:9) and ultrasonic blending for 1 h to form a homogeneous dispersion. 10 µL of the electrocatalyst ink was transferred onto a pre-cleaned surface of the glassy carbon electrode. Similarly, the commercial Pt-loaded carbon electrocatalyst (Vulcan XC-72R) was prepared for comparison according to the same procedure. In all electrochemical measurements, 0.5 M H_2SO_4 aqueous solution saturated with nitrogen/oxygen was used as the electrolyte. The electrochemical measurements were carried out in a potential rage of 0.05 V to 1.2 V at a potential sweep of 50 mV s^{-1} under a constant temperature of 25 °C. In order to get stable response and get rid of the effect caused by Nafion, the continuous potential cycling was performed before the recording of experimental curves. The fresh electrolyte solution was being used in each experiment to ensure the repeated results. IR correction was performed prior to the experiments and RHE correction was also performed after recording the LSV curves. According to the Nernst equation, the measured potentials vs Ag/AgCl (3 M KCl) were converted to the reversible hydrogen electrode (RHE) scale,

$$E_{RHE}=E_{Ag/AgCl}+0.059pH+E°_{Ag/AgCl} \quad (1)$$

Where, $E_{Ag/AgCl}$ is the experimentally measured potential vs Ag/AgCl reference and $E°_{Ag/AgCl}$=0.21 at 26 °C. The potential values provided along the text are referenced against RHE unless otherwise stated.

Results and Discussion

Though structurally perfect graphene exhibits good electron transfer properties, it is not suitable as an electrocatalyst due to the lack of active sites. Moreover, graphene-based electrocatalysts tend to undergo restacking during their preparation and subsequent fabrication of electrodes, which adversely affects the performance due to decrease in surface area and inaccessible electrocatalytic active sites. Therefore, fabrication of stable three-dimensional porous structure of graphene can overcome these shortcomings. Schematic illustration of the synthetic strategy adopted for the fabrication of 3D-Pt@N-doped graphene foam for preparation of proficient electrocatalyst toward ORR is depicted in Figure 1. During oxidation process of graphite, various oxygen-containing groups such as hydroxyl, epoxy and carbonyl groups are introduced into the basal plane carbon atoms of the graphitic structure, whereas the carboxyl groups are introduced at the edges. Moreover, the water molecules could be intercalated within the stack of graphene oxide layers which increases the basal spacing between atomic layer as compared to pristine graphite[48]. Further chemical reduction process converted graphene oxide into graphene, resulting in the significant restoration of sp^2 carbon sites. Meanwhile, the brown colored solution changed into black which was found to be less hydrophilic due to the removal of oxygen-containing groups. The two-dimensional graphene sheets were subsequently integrated with PU sponge by in-situ cross-linking, self-assembly. Nitrogen doping was carried out under hydrothermal treatment in the presence of urea, hydrazine hydrate and ammonia. The driving force for self-assembly was mainly due to the hydrophobic interactions and π- π stacking between graphene layers[49]. Subsequent thermal treatment at high temperature leads to the formation of highly interconnected and continuous porous framework of 3D-N-graphene foam. Recent studies have demonstrated that the introduction of N species creates strong interactions between Pt and the carbon supports that prevent from the aggregation of precious metal particles[50,51]. Hence, Pt nanoparticles were successfully incorporated on nitrogen-doped graphene sheets through hydrothermal method adopting ethylene glycol reduction. More detailed reaction mechanism for the preparation of 3D-Pt@N-Graphene foam with various nitrogen states is illustrated in supporting information (Figure S1).

The formation of graphene oxide and nitrogen-doped graphene leached out from the foam were analyzed by UV-Vis absorption spectroscopy. As displayed in Figure S2, graphene oxide showed a strong absorption peak at 230 nm and a shoulder band at 305 nm which correspond to transition of π-π* from C=C bond and n-π* from C=O, respectively[52]. In nitrogen-doped graphene (N-Graphene), the transition band of π-π* was found to be shifted to 271 nm and notably, the visible absorbance range was increased which revealed the restoration of electronic conjugation due to the removal oxygen functional groups. Figure S3 compare the powder XRD patterns of graphene oxide, graphene, nitrogen-doped graphene and Pt@N-Graphene. The interlayer spacing (3.34 Å) of graphite is reported at a 2θ value (002) of 26.5° (JCPDS # 656212), whereas the graphene oxide peak was found to be shifted from 26.5 to 12.1° corresponding to the increase of interlayer spacing value from 0.33 to 0.73 nm. The drastic increase in interplanar spacing is mainly due to the presence of oxygenated functional groups (hydroxyl, carboxyl and epoxy) and the intercalated solvent molecules during the complete oxidation process (Improved Hummers method).

View Article Online
DOI: 10.1039/C8SE00552D

Journal Name

ARTICLE

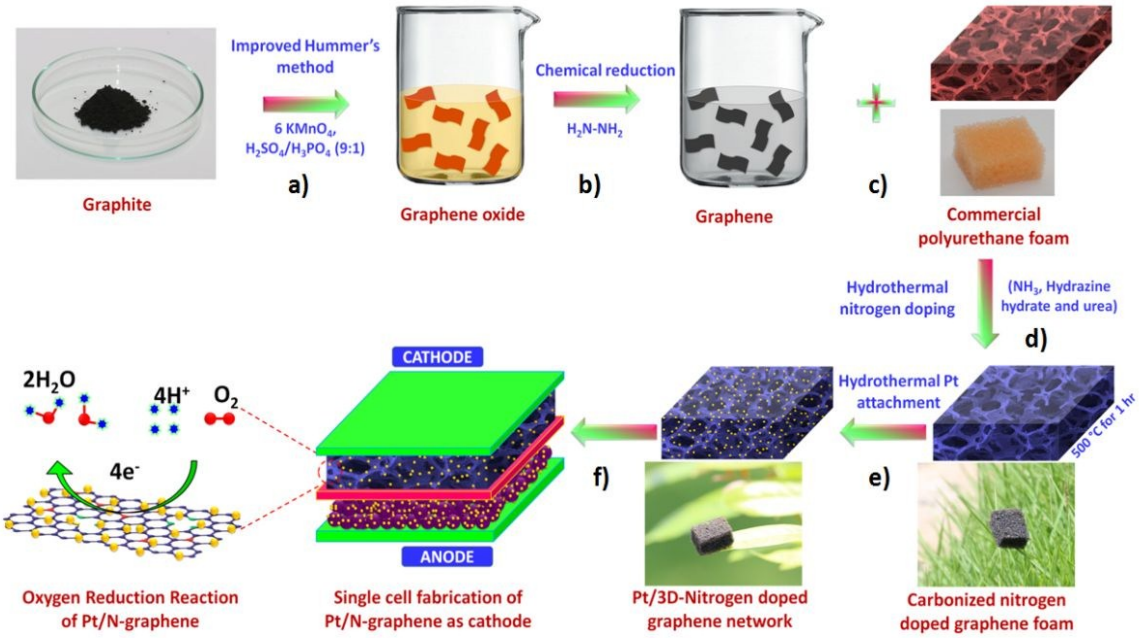

Figure 1. Schematic depiction of the fabrication of 3D-Pt@N-Graphene foam including: a) graphene oxide synthesis via chemical oxidation using improved Hummer's method; b) chemical reduction of GO with hydrazine; c) immersion of commercial sponge into graphene solution; d) Assembly of graphene sheet on the PU skeleton and nitrogen doping by hydrothermal method followed by carbonization; e) hydrothermal attachment of platinum nanoparticles on N-graphene foam and f) assembly of single PEM fuel cell using 3D-Pt@N-Graphene foam based MEA.

As expected with exfoliation of graphene oxide using chemical reduction, original graphitic with a broad peak (002) located at 24.9° corresponding to the *d*-spacing value of 0.35 nm was appeared, which confirmed the recovery of π-conjugated systems. However, N-Graphene synthesized from hydrothermal method with an optimum concentration of urea, ammonia and hydrazine hydrate method showed a peak at 25.9° corresponding to an interlayer spacing of 0.34 nm. The decrease in the interlayer spacing of N-Graphene near to graphitic layer (3.34 Å) is mainly due to further exfoliation of graphene by de-oxidation. The nitrogen doping causes replacement of bulky oxygen-rich surface groups from the basal plane of the carbon framework, which leads to increased structural distortion within the carbon basal plane. Furthermore, all the samples except graphene oxide showed a less profound broad peak around 45° for (100) plane. These results indicated the formation of few atomic layers stacked graphene nanosheets with recovery of graphitic crystal structure. In addition to the broad peak of N-Graphene (002), it should be pointed out that 3D-Pt@N-Graphene showed five dominant diffraction peaks at 39.9, 46.2, 67.8, 81.6 and 85.8 corresponding to (111), (200), (220), (311) and (222) reflections of face centred cubic lattice structure of Pt (JCPDS # 040802). The average crystallite size of the Pt nanoparticles was calculated using Debye-Scherrer formula as 2.4 nm. Pt has a face-centered cubic (fcc) crystal structure and the results suggested that the high density of atomic steps, ledges, kinks and high-indexed crystallographic planes of Pt can exhibit an enhancement in electrocatalytic activity.

The structural changes occurred during chemical processing of graphite to graphene oxide, reduced graphene oxide and nitrogen doped graphene were further supported by Raman spectral analysis (Figure S4). The Raman spectrum of carbonaceous material has been reported with typical two characteristic bands appeared approximately at ~1370 and ~1583 cm-1 for D and G band, respectively[53]. The peak intensity ratio between D bands and G bands (I_D/I_G) is considered as a key parameter mainly used to estimate the degree of defects in the sample. More elaborative studies of graphene oxide and graphene using Raman analysis are clearly described in supporting information. According to literature, higher D band intensity in N-graphene is an indication of increased defect concentration after nitrogen doping[54,55]. The average sp^2 domain size estimated from I_D/I_G ratio is 1.18 and these defect sites can be more favourable for increasing the attachment of Pt electrocatalysts[50].

View Article Online
DOI: 10.1039/C8SE00552D

Journal Name

ARTICLE

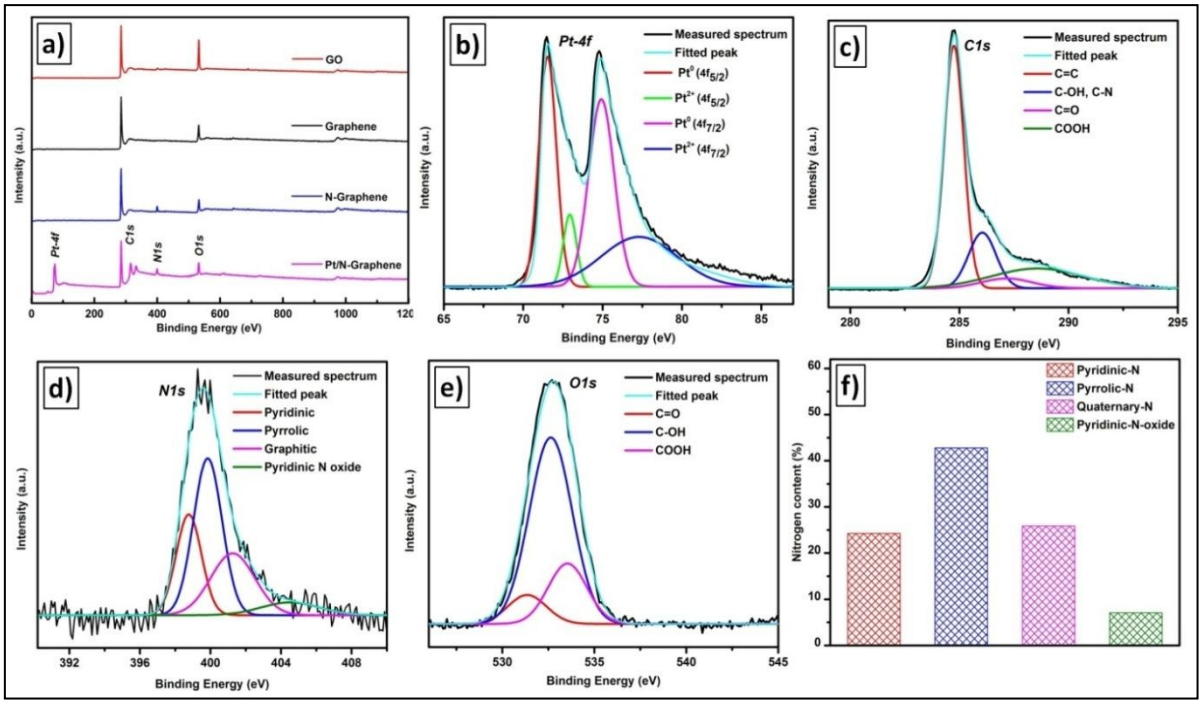

Figure 2. (a) Full survey scan XPS spectra of GO, graphene, N-graphene and 3D-Pt@N-Graphene foam, (b) deconvoluted high resolution XPS Pt4f spectra, (c) deconvoluted high resolution XPS C1s spectra, (d) deconvoluted high resolution XPS N1s spectra and (e) deconvoluted high resolution XPS O1s spectra of 3D-Pt@N-Graphene foam.

The functional groups present in the materials were further investigated by Fourier transform Infrared Spectroscopic (FT-IR) analysis (Figure S5) and thermogravimetric analysis (TGA) (Figure S6) in supporting information[56]. Figure S7 shows the thermal decomposition behaviour of bare PU foam and 3D-Pt@N-Graphene foam under nitrogen atmosphere. As it can be seen, the pristine PU foam showed two obvious weight losses around 250 and 350 °C, respectively. The first stage of weight loss was found to start in the temperature range of ~250 °C suggesting the decomposition (34 %) of urethane group leading to the formation of amine and olefin or to the formation of a secondary amine and carbon dioxide. In the second stage, weight loss was found to be 46 % associated with other segments of the structure (ether or ester links), finally 13 % weight remained as char yield and no noticeable weight loss was observed above 500 °C implying that the PU foam was not completely removed[57]. As shown in Figure S7, the thermogram of 3D-Pt@N-Graphene foam was quite similar to pure PU foam. However, it showed only insignificant weight loss of ~44 % around 200-300 °C and ~ 60 % weight loss until 500 °C leaving behind the 3D conductive network of Pt@N-Graphene and the thermal stability also indicate the stronger chemical interaction between N-graphene and PU skeletons of foam which inhibits this effect [58].

Further investigation of electronic configurations and surface chemical compositions of 3D-Pt@N-Graphene foam based electrocatalyst were deciphered on the basis of XPS results, as illustrated in Figure 2. Figure 2a shows the survey scan of 3D-Pt@N-Graphene and it can be observed that the peaks centered at 285.1, 401, 532.2 and 73.2 eV are assigned to the binding energies of C1s, N1s, O1s and Pt4f, respectively. These results revealed the successful incorporation of N atoms in the lattice of graphene layers, the anchoring of Pt nanoparticles on the graphene sheets and their calculated percentage of platinum in the graphene nanostructure was 7.81 %. As shown in Figure 2b, the recorded high-resolution Pt4f spectrum of 3D-Pt@N-Graphene foam was de-convoluted into two individual components (4f5/2 and 4f7/2). The first most intense doublet Pt4f peaks at 71.5 eV (4f7/2) and 74.9 eV (4f5/2) are attributed to the metallic platinum (Pt0), indicating that most of Pt ions were completely reduced to the metallic state of Pt. The second set of doublet Pt4f peaks at 72.9 eV (4f7/2) and 76.8 eV (4f5/2) are emerged due to platinum oxide and platinum hydroxide (Pt^{2+}) species. The calculated percentage of Pt0 measured based on the relative area is 89.8 %. A small quantity of Pt(II) species may be originated from the adsorbed oxygen on the Pt. As evident from Figure 2c, the predominant narrow graphitic C1s peak was further

deconvoluted into four individual components, such as C=C, C-OH/C-N, C=O and O–C=O from the corresponding peaks observed at 284.7, 286.1, 287.2 and 288.5 eV, respectively. Notably, the identification of C-N peaks in C1s high-resolution spectrum confirmed the incorporation of nitrogen atoms within the graphene layers. As displayed in high-resolution C1s spectrum of N-rGO samples, the peak corresponding to C-C bond is tremendously stronger than those of other C-O, C=O, O-C=O peaks. It should be noticed that the N-Graphene based samples contain a small number of oxygen-containing functional groups because of the reduction induced by nitrogen doping process[59]. Furthermore, N/C atomic ratio estimated from XPS results was approximately 8.17 atomic %, as summarized in Table S2. On the other hand, typical high-resolution N1s spectrum (Figure 2d) was de-convoluted into four characteristic peaks centered at 398.7, 399.8, 401.2 and 403.8 eV which can be ascribed to pyridinic-N (N atom on the edge of the graphitic planes with two adjacent carbon atoms imparting Lewis basicity to carbon), pyrrolic-N/pyridonic-N (N atom contributes to π conjugated system with a pair of p-electron with a relatively lower binding energy), quaternary-N (carbon atom in the graphene hexagonal-ring substitute by the N atoms with a relatively higher binding energy) and pyridinic oxide-N, respectively. As displayed in Table S2, the relative amount of these four N species were calculated to be 24.6, 42.7, 24.8 and 7.8 % for pyridinic-N, pyrrolic-N, graphitic-N and pyridinic oxide-N, respectively. The exact mechanism of nitrogen-modified carbon supports toward ORR is not clearly identified, but still the active sites are generally thought to be quaternary-N atom bonded to three carbons, pyridinic-N and pyrrolic-N [60,61]. Therefore, it is strongly believed that the ORR electrocatalytic performance also depends on the increase in carbon π states and the presence of edge defects in the graphene lattice, such as pyridinic N and pyrrolic N [33,62,63]. Moreover, the graphitic nitrogen bonded with three carbon atoms (sp2) is supposed to display higher electro negativity (3.04) than that of C (2.55), which facilitated the electronic conductivity as well as the adsorption of O_2 on the electrocatalyst, that also contributed to the enhancement of electrocatalytic activity[60,64,65]. In contrast, pyridinic oxide-N type nitrogen is unstable under fuel cell operating conditions which does not significantly contribute to the ORR performance [66]. The fitting of high resolution O1s spectra (Figure 2e) yielded three peaks at 531.4, 532.6 and 533.5 which are responsible for C=O, C-OH and COOH. The results observed from O1s spectra is in accordance with the results obtained from C1s and N1s spectra. Therefore, the presence of high content metallic state of Pt and nitrogenous species such as, pyridinic, pyrrolic and graphitic groups are highly desirable and more beneficial for improving electrocatalytic activity toward ORR, which is discussed in the following sections.

Transmission electron microscopy (TEM) was used to investigate the surface morphology and microstructure of as-synthesized graphene oxide, graphene, N-graphene and Pt@N-Graphene stripped out from the 3D-Pt@N-doped graphene foam. As displayed in Figure S8, graphene oxide sheets were highly opaque and thick, manifesting that graphene layers are restacked each other, whereas, graphene sheets after reduction were thin transparent layers with wrinkles and folds indicating their restacking free property [51,67].

As can be seen from Figure 3a, the transparency of N-doped graphene was furthermore increased and it was found to be very thin, transparent and wrinkled morphology with some dark ripples due to the pliability. This transparency indicated that the nanosheets are having only a few layers and the thicker ripples due to the crumpling of nanolayers. As shown in Figure S8 (inset), the selected area electron diffraction (SAED) provides a ring-shaped pattern consisting of sharp diffraction spot for each order of diffraction which make hexagons with different rotational angles, implying the overlapping of graphene nanosheets. These results directly implied that the presence of large amount of free space between graphene layers which can facilitate excellent transport of electrons. Unlike the hexagonal patterns of graphene, nitrogen-doped graphene sample showed a ring diffraction pattern with bright spots, indicating the structural distortion caused by the intercalation of nitrogen atoms in the basal plane of graphene, as observed in previous reported literatures [50,62]. The corresponding d-spacing of graphene oxide, graphene and nitrogen-doped graphene were calculated to be 0.732, 0.351 and 0.343 nm.

As can be seen from Figure 3b-d, it is clearly identifying the uniform distribution of Pt nanoparticles without aggregation. In addition, Figure 3e demonstrates the corresponding dark-field TEM image of Pt/N-Graphene and the clear bright spot is also showing the distribution of platinum nanoparticles on a thin layer of graphene sheet. The average size estimated by measuring more than 100 Pt nanoparticles in the TEM images of 3D-Pt@N-Graphene foam was about 2.82 nm which is relatively closer to that Scherer analysis discussed in XRD analysis and their narrow size distribution is illustrated in Figure 3c (inset). Meanwhile, the presence of smaller sized uniform Pt nanoparticles are mainly because of the nitrogen doping over graphene surface [11]. Moreover, theoretical investigations corroborated that the introduction of N species in carbon skeleton improves the interaction between Pt and supports, which prevent from agglomeration of Pt nanoparticles[50]. Besides, Figure 3f also indicates the atomic lattice fringes of Pt nanoparticles in N-graphene and the d-spacing of Pt (111) plane was found to be that 0.229 nm. The presence of spot patterns in 3D-Pt@N-Graphene indicated their polycrystalline nature. The spots were indexed based on the JCPDS database (87-0646) and the results indicated that Pt has a face-centered cubic (fcc) crystal structure which is in accordance with XRD results.

Figure S9 (supporting information) shows the representative atomic force microscopic (AFM) images of graphite, graphene oxide, graphene and nitrogen doped graphene. The sample used for these studies were drop casted films of its aqueous dispersion on silicon wafer surface. The layered structure revealed in Figure S9 (inset) which enabled us to determine the thickness of graphene oxide, graphene and N-graphene by using line scan profiles across the sheets.

View Article Online
DOI: 10.1039/C8SE00552D

Journal Name

ARTICLE

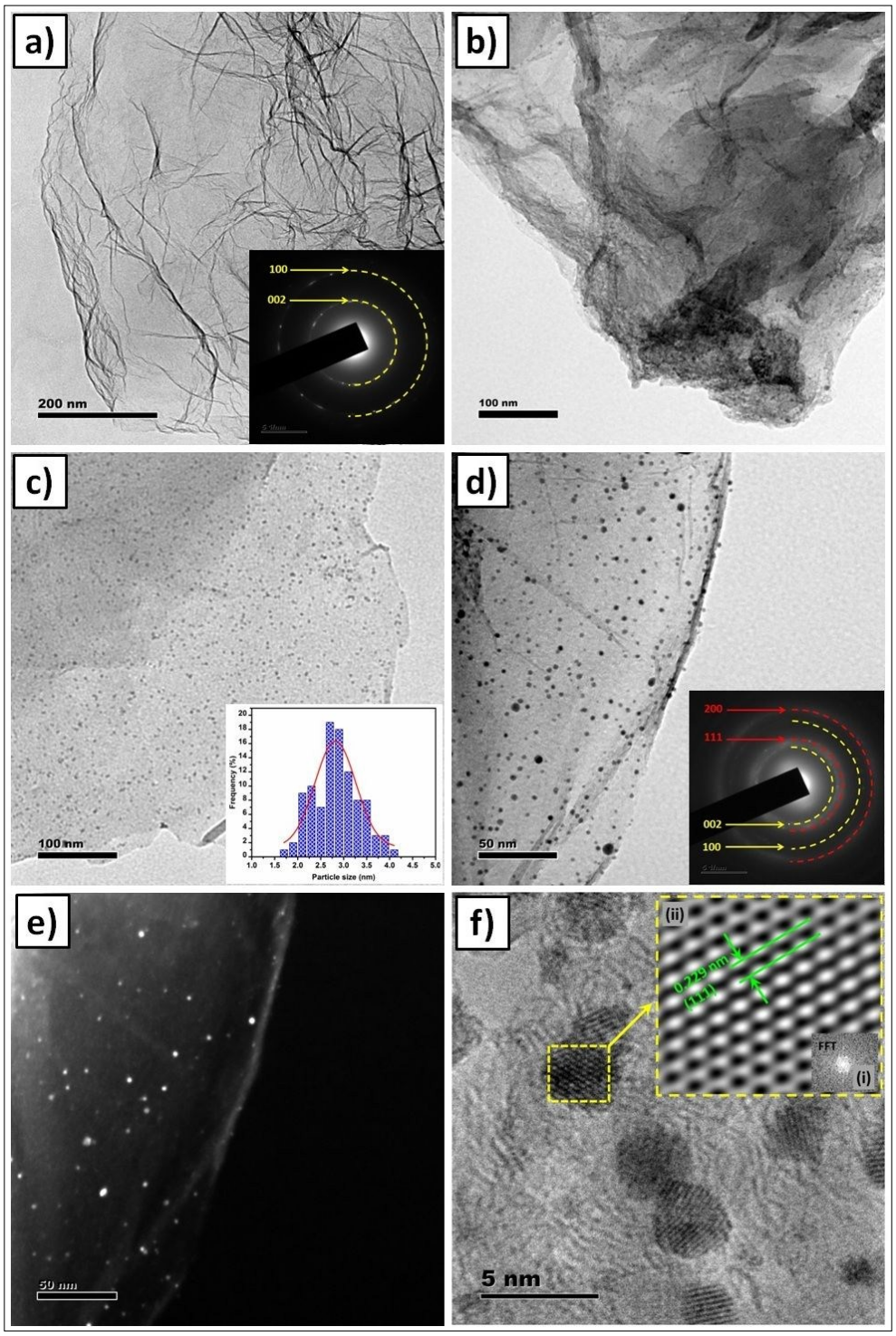

Figure 3. TEM images of (a) N-graphene (Inset shows the SAED patterns and their scale bar corresponds to 5 nm^{-1}), (b-d) 3D-Pt@N-Graphene and SAED pattern of 3D-Pt@N-Graphene and their corresponding (e) dark field image and (f) high resolution TEM images of 3D-Pt@N-Graphene (Inset: (i) Fast Fourier Transformation image (FFT) and (ii) Inverse Fourier-filtered image of square marked area).

View Article Online
DOI: 10.1039/C8SE00552D

Journal Name

ARTICLE

The graphite flake (Figure S9a) showed a rough morphology with thickness and lateral dimensions as 600 nm and 4-6 µm, respectively. The graphene oxide nanosheets were mainly comprised of few layers of graphene nanosheets having an average thickness of 5 nm and lateral dimension typically between a few and several hundreds of nanometres. As a representative example, graphene nanosheets showed a thickness of 3 nm with a lateral dimensions ranging from several hundred nanometres to several micrometers. Similarly, N-doped graphene nanosheets possessed a flat sheet-like structure with an apparent thickness ~1-1.5 nm and no noticeable change was observed in the lateral dimension of graphene sheets. These results suggested that N-graphene had very thin morphology which is the characteristic of complete exfoliation of carbon sheets and majority of the sheets are single atomic layer objects.

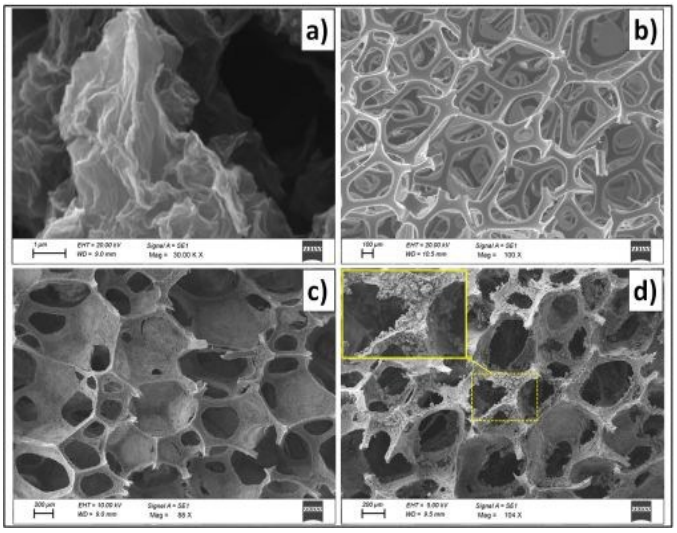

Figure 4. SEM micrographs of N-Graphene (a), bare PU foam (b) and Pt@N-Graphene coated on PU foam (c) and carbonized 3D-Pt@N-Graphene foam (d).

In order to fabricate a large area conductive network and electrochemically active foam, we used nitrogen graphene nanosheets as the conductive coating on PU scaffold and their detailed structure and morphology were investigated using scanning electron microscopy (SEM). The SEM images of graphite, graphene oxide and graphene are shown in Figure S10 which revealed the exfoliation of graphene layers. As can be seen from Figure 1 and 4a, the flame-like N-doped graphene exhibited a mechanically flexible structure. Figure 4 (b-d) shows the morphology of the three-dimensional porous foam constructed from Pt@N-Graphene and the bare porous PU sponge. As shown in Figure 4b, the bare PU sponge showed a very smooth surface, interconnected, highly porous 3D networks with many macro pores of hundred micron size. After dip coating with N-doped graphene, it is evident that the graphene layer ripples and wrinkles and were self-assembled, cross-linked and completely wrap around the skeleton of PU sponge. The N-doped graphene content could be readily tuned by varying the loading levels during the fabrication process and it was found that the coating roughness of the three dimensional foam increased with increasing concentrations of Pt@N-Graphene. It also illustrated that the hydrothermal reaction did not cause any deterioration to PU sponge which can effectively hamper the aggregation and restacking of graphene layers. Moreover, it is evident that very thin and interconnected graphene layers are tightly connected to form a 3D structure that can prevent aggregation. After pyrolysis (Figure 4d) under nitrogen atmosphere, the carbon skeleton was retained and they yield strongly intact and stable 3D scaffold structure with porous carbon framework [57].

Although slight shrinkage occurs in the overall texture, the N-doped graphene sheets are still overlapped each other leaving behind three-dimensional conductive networks. Meanwhile, the thicknesses of the pyrolyzed foams were marginally smaller than those of bare PU sponge. Moreover, these results strongly confirm the presence of hierarchical micro/mesopores due to the interconnected Pt@N-Graphene coating in the skeletons of PU. Hence, SEM results suggested that the hierarchical 3D porous structure supports have a crucial advantages of large porosity that makes easy flow of reactants, smooth inner and outer surface of polyhedron open cell structure facilitate the uniform dispersion of Pt nanoparticles and reconstructed graphene network (sp^2 carbon structure) in these skeletons are free from the inter-junctions that provides superior electron transporting pathways. Therefore, this hybrid nitrogen-doped graphene foams could be regarded as an ideal support material for fuel cell applications. From the above results it is clear that 3D-nitrogen doped graphene foam gives a highly porous interconnected conducting scaffold for anchoring uniformly distributed of Pt nanoparticles having narrow size range (2-3 nm). The N-doped graphene foam have abundant defective sites in the form of edge atoms of pyridinic and pyrrolic type nitrogen species (as revealed from XPS analysis) present on the surface, which are responsible for its high performance. Generally, the pyridinic nitrogen atoms tend to locate at the edges of the graphitic layers in the foam which is a huge 3D porous network. As the electronic structure of the graphene used for the 3D foam development was modified by N-doping process, the Pt nuclei were readily attached to these active sites during hydrothermal polyol reduction.

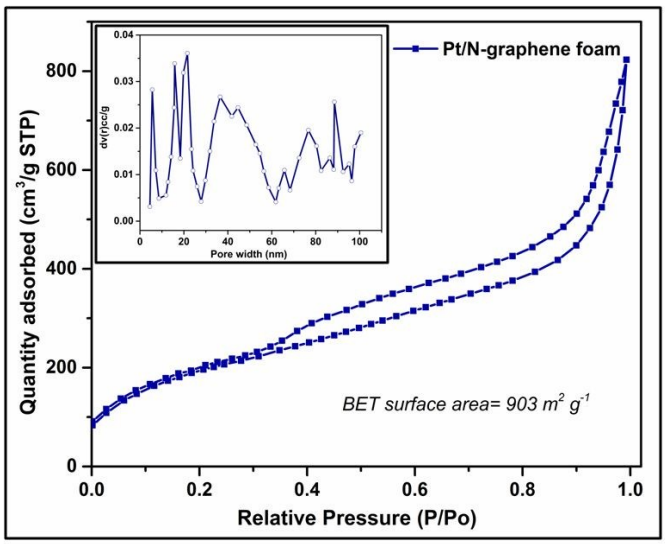

Figure 5. BET nitrogen adsorption-desorption isotherm; Inset shows the pore size distribution (NLDFT model) of 3D-Pt@N-Graphene foam.

In order to further characterize the surface area and porous structure of 3D-Pt@N-Graphene foam, N_2 adsorption-desorption measurements were employed. Figure 5 display a typical type IV reversible isotherm curve associated with a distinct H_4 hysteresis loop and a steep uptake of nitrogen at a high relative pressure (P/P_o), demonstrating the existence of macro-mesopores[68,69]. Furthermore, rapid increase in low-pressure region also confirmed the existence of micropores. These results also reflected in pore size distribution plot (inset) which clearly showed a broad range between 1-100 nm, which strongly manifest the co-existence of micropores and mesopores. The obtained pore structure parameters are summarized in Table S3. As summarized in the Table, the calculated specific surface area and total pore volume for 3D-Pt@N-Graphene foam are 903 m^2/g and 0.48 $cm^3 g^{-1}$ respectively. The pore size distribution curve calculated based on NLDFT methods (Figure 5 inset) indicated that the product have few micropores (<2 nm), well-developed mesopores (2-50 nm) and macropores (>50 nm). It is noteworthy that the broader pore size distribution and lack of adsorption plateau at high-pressure region is an indicative of slit-shaped pores in an open pore system. As it can be concluded that, the presence of hierarchical porous network with large specific surface area and high total pore volume in 3D-Pt@N-Graphene foam structure would be more ideal for smooth mass transfer and shorten the diffusion pathways of ORR relevant species; thereby it can contribute to the triple phase boundary enhancement.

The mechanical properties of the porous 3D-Pt@N-Graphene foam were evaluated using cyclic compressive stress (σ)-strain (ε) response curves as depicted in Figure 6. The compression curves (Figure 6a) of Pt@N-graphene foam under various applied strain (20–80 %) showed complete recovery without any structural fatigue. It is evident that a clear elastic deformation with a sharp increase of stress occurred at small strains, resulting from the accommodation of the material into pores of the foam. Moreover, the compression curve (Figure 6b) exhibited rapid increase in stress which further returned to zero, demonstrating fast and nearly complete recovery to its original state even after being subjected to 100 cycles. Besides, the stress–strain curve exhibited three distinct deformation regions; a linear-elastic region (i) for ε < 12 % with an elastic modulus of 0.12 MPa, a plateau yield region (ii) for 6 < ε < 65 % and a steep slope densification region (iii) for ε > 65 %. The excellent compressibility and recoverability of 3D-Pt@N-Graphene foam with small dimensional loss during the cyclic compressive tests suggested the superior flexibility of the material which is mainly due to its high porosity and good elasticity.

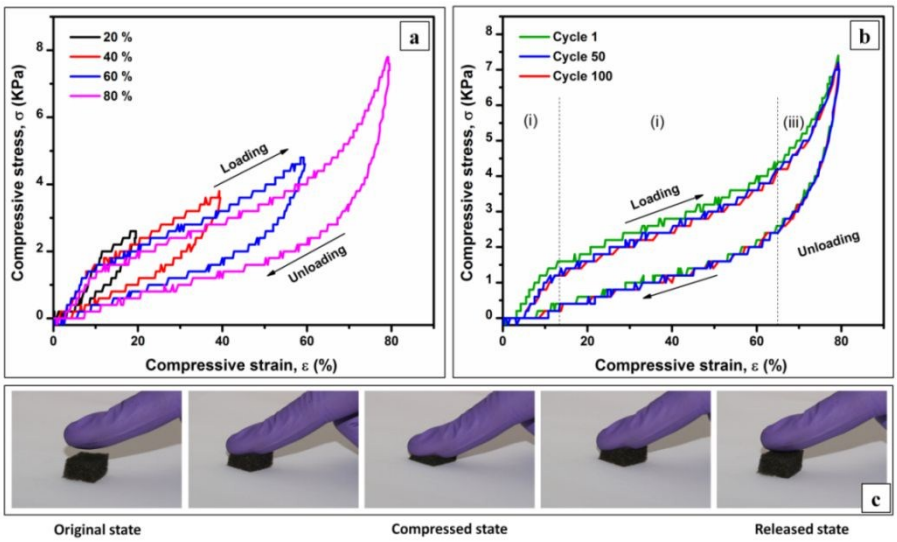

Figure 6. (a) Stress-strain curves of 3D-Pt@N-Graphene foam under various set strain of 20, 40, 60 and 80 %, respectively, (b) Typical cyclic stress–strain response curves of porous 3D-Pt@N-Graphene foam (1, 50 and 100 cycles at a maximum strain of 80 %) and (c) Digital photographs show the compression process displaying excellent compressibility and recoverability.

View Article Online
DOI: 10.1039/C8SE00552D

Journal Name

ARTICLE

Electrochemical studies of 3D-Pt@N-graphene Foam

Numerous efforts have been made on reducing the quantity of noble metal (Pt) catalyst with simultaneous enhancement of ORR performance in fuel cells. Several reports have explored the possibility of metal free N-Graphene itself as a potential candidate for ORR electrocatalyst [28,31,33,34]. To demonstrate the efficient electrocatalytic activity of 3D-Pt@N-graphene foam for ORR, cyclic voltammograms were first obtained using conventional three electrode system in N_2 and O_2 saturated 0.5 M H_2SO_4 at a scan rate of 50 mV. The commercial electrocatalyst, Pt loaded on carbon support (Vulcan XC-72), Pt@N-Graphene and N-graphene also were tested under the similar conditions for comparison. The cyclic voltammograms (Figure 7a) of the prepared electrocatalysts were obtained in 0.5 M H_2SO_4 under nitrogen atmosphere to estimate the electrochemical active surface area of the platinum from the coulombic charge of the hydrogen adsorption/desorption peak (Q_H). The electrochemical surface area of the prepared electrocatalysts was calculated by using the following relation[70],

$$ECSA = Q_H/[Pt] \times 0.21 \quad (2)$$

Where, Q_H (mC) is the charge due to the hydrogen adsorption/desorption region from CV, [Pt] represents the loading amount of Pt on the working electrode and 0.21 mC cm^{-2} is the charge required to oxidize a monolayer of H_2 on Pt site[71,72]. The calculated ECSA (Table S4) of 3D-Pt@N-Graphene foam (84.9 m^2 g^{-1}) is approximately 1.2 times higher than that of Pt@N-Graphene (74.63 m^2 g^{-1}) and 1.6 times greater than that of commercial Pt/C (53.3 m^2 g^{-1}) electrocatalyst. The higher ECSA of 3D-Pt@N-Graphene foam compared to Pt@N-Graphene and commercial Pt/C is mainly attributed to the uniformly distributed smaller sized platinum nanoparticles and incorporation of nitrogen atoms in the carbon lattice.

In order to examine the electrocatalytic activity of the 3D-Pt@N-Graphene foam over other electrocatalysts, the ORR tests were performed by cyclic voltammetry in 0.5 M H_2SO_4 solution saturated with oxygen at a scan rate of 50 mV/s. Figure 7b, shows well-defined more positive cathodic peak centred at 0.85 V and a dramatic increase in voltammetric current for 3D-Pt@N-Graphene foam as compared to other electrocatalysts (Pt@N-Graphene (0.84 V) and Pt/C (0.83 V)). This strong response of 3D-Pt@N-Graphene foam demonstrated the pronounced electrocatalytic activity toward ORR. For further evaluation and comparison of electrocatalytic activity of 3D-Pt@N-Graphene foam over other electrocatalysts, linear sweep voltammograms were acquired through rotating disk electrode (RDE) measurements at 1600 rpm. Figure 7c show the polarization curves of various electrocatalysts and 3D-Pt@N-Graphene foam exhibited highly positive onset potential (53 mV), half wave potential (62 mV) and high mass transport limiting current density (4.68 mA/cm^2) (Table 1) at 0.4 V which is comparatively higher than that of Pt@N-Graphene, commercial Pt/Vulcan carbon and N-graphene electrocatalysts over a large potential range. The obtained ORR results were compared with the reported Pt/C electrocatalysts in various electrolytes (Table S5). This observation could be attributed to the faster ORR kinetics with a larger transferred number of electrons per oxygen molecule. Therefore it is expected that the 3D-Pt@N-Graphene foam structure can result in increased electrocatalytic activity toward ORR and that could be explained with the excellent electron transport properties and increased electrochemical surface area of the material. Surprisingly, 3D-Pt@N-Graphene foam electrocatalyst exhibited superhydrophilic properties. Ultra-hydrophilicity has been found to form an easily wetted surface which first ensures a high dispersion of metal-related active sites and also increases the accessibility of reactants to active centres, and thus increase surface and mass utilization efficiency of catalysts (Figure S12)[44]. Moreover, the dimensionality evolution of two dimensional (2D) Pt@N-graphene to a complex three dimensional (3D) structure as 3D-N-graphene foam generates very high surface areas and highly exposed tangles and edges that contain large number of active sites, which is responsible for the superior fuel cell performance. The 3D foam structure of the electrocatalyst support membrane, owing to its highly porous networked structure augments the triple phase boundary (TPB) sites, which are the interfaces, where the electrolyte, gas, and electrically connected catalyst come into contact. The electrochemical reaction can only occur at TPB's when these zones are properly connected each other and 3D foam structure of the catalyst support material provides suitable platform for abundant TBP sites throughout the porous network.

Table 1. LSV measurement parameters.

Material	Onset potential (mV)	Limiting current density mA/cm^2 (at 0.4 V)	Half wave potential (mV)
3D-Pt@N-Graphene foam	989	4.675	895
Pt@N-Graphene	973	4.449	874
Pt/C	936	4.090	833
N-graphene	919	2.741	805

View Article Online
DOI: 10.1039/C8SE00552D

Journal Name

ARTICLE

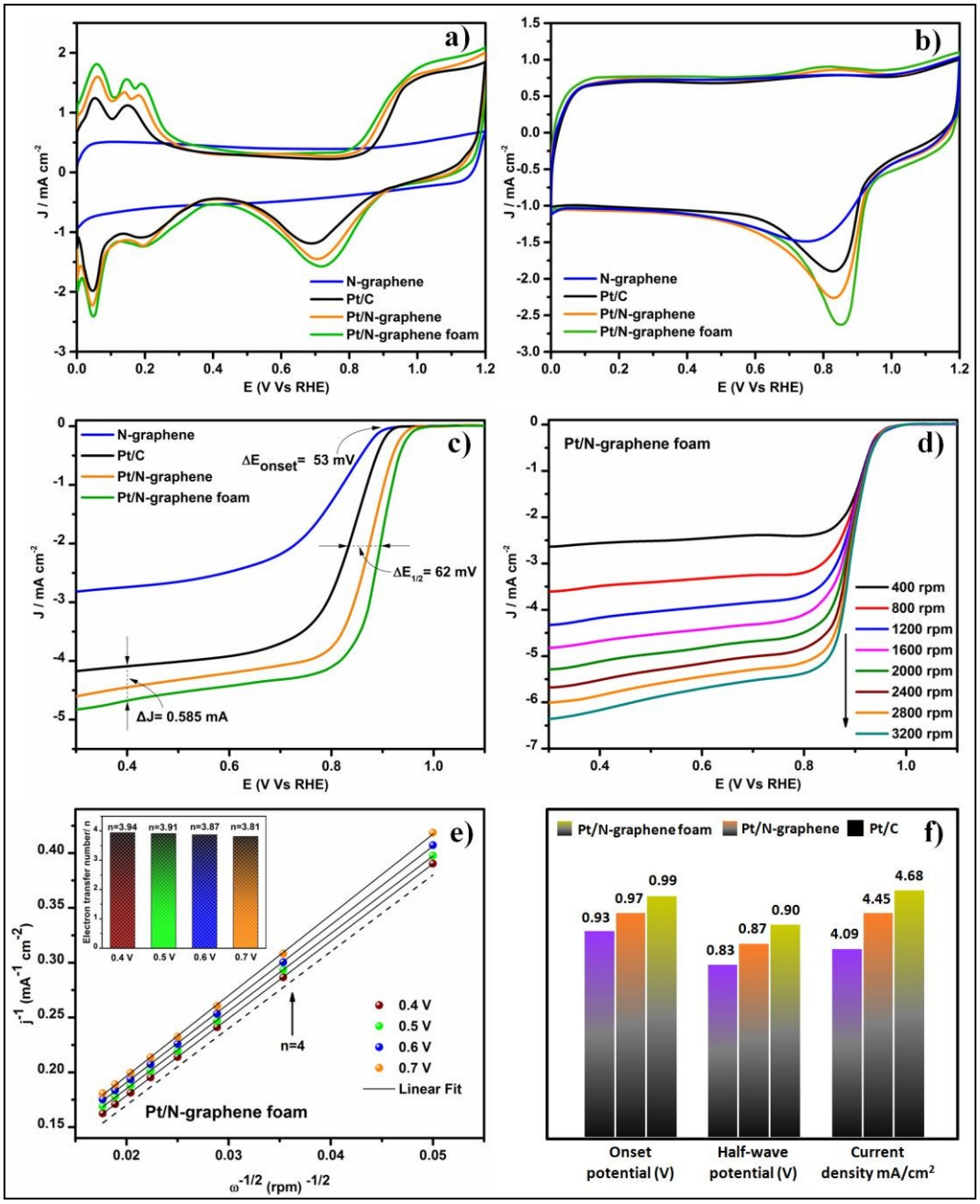

Figure 7. (a) Cyclic voltammogram of 3D-Pt@N-Graphene foam, Pt@N-Graphene, N-graphene and commercial Pt/C in N_2 saturated H_2SO_4 at a scan rate of 50 mV s^{-1}, (b) Cyclic voltammogram of 3D-Pt@N-Graphene foam, Pt@N-Graphene, N-graphene and commercial Pt/C in O_2 saturated H_2SO_4 at a scan rate of 50 mV s^{-1}, (c) Rotating disk electrode (RDE) linear sweep voltammograms (LSV) of ORR of various electrocatalysts with a rotation rate of 1600 rpm at a scan rate of 10 mV s^{-1}, (d) RDE LSV curves of ORR for 3D-Pt@N-Graphene foam electrocatalyst with a different rotation speeds (400-3200 rpm) at a scan rate of 10 mV s^{-1}, (e) Koutecky- Levich plots (j^{-1}vs$\omega^{-1/2}$) of 3D-Pt@N-Graphene foam obtained from different potentials of RDE LSV curves and (f) electrocatalytic activity given as onset potential, half-wave potential and limiting current density at 0.4 V of all three electrodes.

In order to gain better insight into the electrocatalytic reaction kinetics mechanism, linear sweep voltammetry was used (Figure 7d) for 3D-Pt@N-Graphene foam by employing rotating disc electrode (RDE) at various rotating speeds (400-

3200 rpm) at a scan rate of 10 mV/s. The limiting current density of oxygen reduction reaction was found to be increased with increasing in rotation speed which is mainly caused by the shortest diffusion distance at high speeds. The oxygen reduction reaction performances in the kinetic and diffusion regions were determined using the Koutechy-Levich (K-L) plots, as depicted in Figure 7(e).

The corresponding K-L plots (J^{-1} vs $\omega^{-1/2}$) of 3D-Pt@N-Graphene foam at various electrode potentials demonstrated good linearity and parallelism which indicated first-order reaction kinetics with respect to dissolved oxygen concentration. Fundamentally, the mechanism of ORR in acidic media is mainly regarded as a multi-electron charge transfer reaction which can occur either through one step pathway involving four electron transfer for direct conversion of oxygen into water ($O_2+4H^++4e^-\rightarrow 2H_2O$) or two step pathway involving two electron transfer for converting oxygen into H_2O_2 ($O_2+2H^++2e^-\rightarrow H_2O_2$) and further converting into H_2O ($H_2O_2+2H^++2e^-\rightarrow 2H_2O$) by another two electrons[31]. In other words, two electron reduction occurs at a higher potential (low over potential absolute value), where the adsorbed intermediate species are related to be O_{ads}, OH_{ads} and OOH_{ads}, in which OOH_{ads} is formed initially and then the O-O bond is being broken. In contrast, four electron transfer occurs at a lower potential, while the ORR follows a direct dissociation mechanism in which the O-O bond is broken before OH_{ads} is formed [6,73]. Here, the one step four electron transfer associative direct pathway is more desirable for ORR activity and other is less efficient two-electron pathway [23,74]. Electron transfer number (n) per oxygen molecule involved in the ORR process was calculated according to the following equations,

$$\frac{1}{j}=\frac{1}{j_{diff}}+\frac{1}{j_{kin}}=\frac{1}{jB\omega^{1/2}}+\frac{1}{j_{kin}} \quad (3)$$

$$B=0.62nFC_{O_2}(D_{O_2})^{2/3}\upsilon^{-1/6} \quad (4)$$

$$j_{kin}=nFkC_0 \quad (5)$$

Where, j is the measured current density, j_{kin} and j_{diff} is the kinetic and diffusion-limiting current densities, ω is the angular velocity of the rotating disk electrode (ω=2πN). N is the linear rotation speed) and n is the transferred number of electrons that is exchanged during the ORR process, F is the Faraday constant (96,485 C/mol), Do_2 is the diffusion coefficient of O_2 in H_2SO_4 electrolyte (1.8 x 10^{-5} cm^2 s^{-1}), Co_2 is the bulk concentration of O_2 (1.13 x 10^{-6}mol cm^{-3}), υ is the kinematic viscosity of the electrolyte (0.01 cm^2 s^{-1}) and k is the electron transfer rate constant[31]. The electron transfer number (n) in ORR for 3D-Pt@N-Graphene foam electrocatalyst was calculated as 3.7 over the potential range of 0.4 to 0.7 V, inferring that most of the molecular oxygen was reduced onto water following a one step, four-electron transfer pathway and this phenomenon showed high selectivity towards ORR activity. The doping of nitrogen in the carbon sites introduces defects, which result in the structural distortions in graphene lattice. Based on quantum mechanical aspects, the substituted nitrogen atoms in the carbon sites behave as an electron acceptor sites and form the electron acceptor state in the conduction band near the Fermi level. It should be noted that the presence of nitrogen in the graphene lattice introduces the charge density and asymmetry in spin density which promotes the charge transfer from the support material to adsorb oxygen molecules. This facilitates the dissociation of O-O bond by weakening them enhances the ORR activity [11,35,75,76]. Moreover, the combination of graphitic-N, pyridinic–N and pyrrolic-N present in nitrogen-doped graphene are more favourable for ORR[77]. Particularly, the formation energy is relatively low when the dopant is located at the edges (Pyridinic-N) which is more favourable for achieving low over potential for ORR due to the easier adsorption of O_2 leading to the ease enhancement of ORR. Therefore, the high selectivity towards water also results in maximum current generation and less corrosion problems caused by the absence of hydrogen peroxide[31]. Nitrogen doping in graphene network is not only beneficial for the dispersion of catalyst nanoparticles, but also prevent agglomeration by stabilizing them. The 3D foam structure also prevents the irreversibly aggregation of graphene sheets enhancing the electrocatalytic properties and also facilitates the mass transport properties. The highly interconnected porous networks in 3D-graphene foam are big enough for the diffusion of reactant gas and favorable for the Nafion ionomers to penetrate and contact with the catalyst particles of PEMFCs. Compared to the traditional 2D electrocatalyst support materials, the conductive network and high specific area of 3D support materials can provide more anchoring sites for electrocatalysts for effective electron transfer by reducing the ion diffusion length. Therefore, it is strongly emphasized that the unique characteristics of 3D structure and interconnected porous network with mesopores and nitrogen doping leads to abundant triple phase boundary sites by means of facilitating the large contact area between electrocatalyst and electrolyte, more space to accommodate any volumetric expansion, high specific surface offered more anchoring sites for Pt nanoparticles, favorable conditions for adsorption of gas molecules, diffusion and efficient mass transport in the active catalytic sites and graphene network provided a large number of conductive pathways to achieve fast electrochemical reaction. Hence, the excellent activity of 3D-Pt@N-Graphene foam would make them a promising candidate as electrocatalyst for ORR in PEM fuel cells.

Stability Studies

The stability of the electrocatalyst over several cycles is one of the decisive factors for their implementation practical applications in fuel cells. In order to evaluate the electrochemical stability of 3D-Pt@N-Graphene foam electrode toward ORR, chronoamperometric (CA) response at 0.6 V and accelerated durability test (ADT) protocol using linear sweep voltammetry tests were conducted in O_2-saturated 0.5 M H_2SO_4. As indicated in Figure 8a, the 3D-Pt@N-Graphene foam demonstrated only a slight attenuation of current density (14%) at 0.6 V over other two electrocatalysts such as, Pt@N-Graphene (19%) and commercial Pt/C (33%). The Chronoamperometry results of 3D-Pt@N-Graphene foam based electrode clearly indicated that there was no significant loss in the current density with increasing time and the

electrode could even retain 85% of its initial current density. On the other hand, the chronoamperometric response of commercial electrocatalyst (Pt/Vulcan carbon) showed a gradual decline from its initial current density. Similarly, it can also be observed from linear sweep voltammetry that 3D-Pt@N-Graphene foam based electrocatalysts showed only 24 mV negative shift on its half-wave potential after 10000 cycles. In contrast, the commercial catalyst displayed 75 mV loss under the same conditions. Hence, these findings suggest that the 3D-Pt@N-Graphene foam based electrocatalysts has excellent long-term stability compared to other two electrocatalysts. The structural and compositional stability of the 3D-Pt@N-Graphene foam after the durability testing was further confirmed by TEM and XPS analysis (Supporting information, Figure S11).

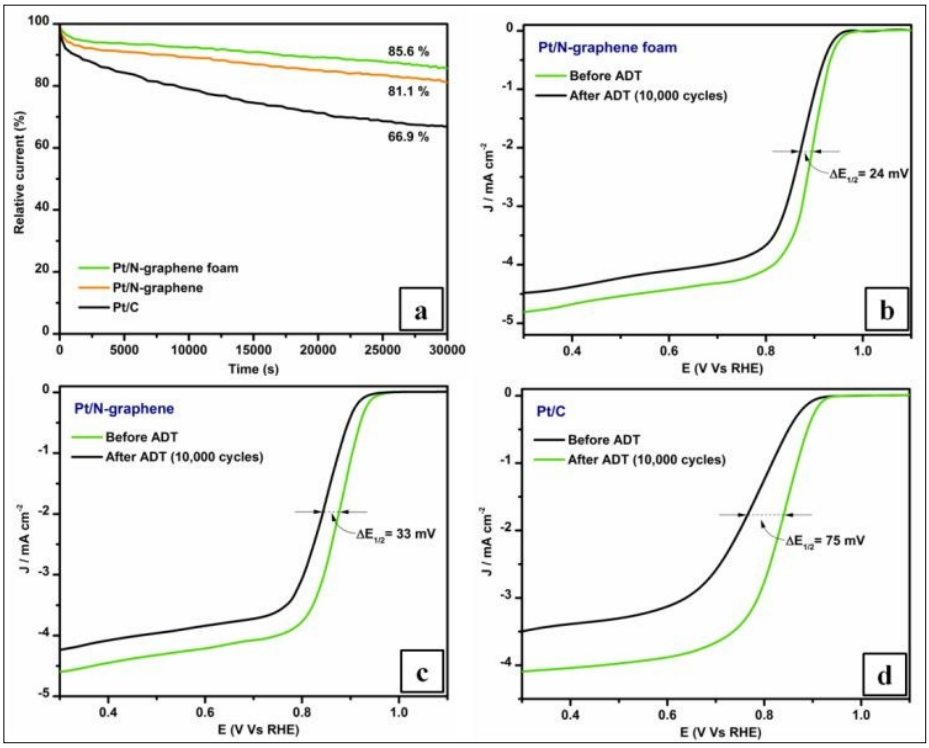

Figure 8. Electrochemical stability studies from the (a) current–time (j–t) chronoamperometric responses of 3D-Pt@N-Graphene foam, Pt@N-Graphene and Pt/C for 30,000 s in O_2-saturated 0.5 M H_2SO_4 at a constant potential of 0.6 V and (b-d) LSV curves 3D-Pt@N-Graphene foam, Pt@N-Graphene and Pt/C on RDE (1600 rpm) before and after 10,000 potential cycles in O_2-saturated 0.5 M H_2SO_4 at a scan rate of 10 mV/s.

Single Cell testing

Besides their superior ORR performance in acidic media, it is very essential to demonstrate their performance in actual PEM fuel cell. Figure 9 demonstrates the polarization curves obtained from single cell test results when the 3D-Pt@N-Graphene foam, 3D-Pt@ graphene foam, Pt@N-Graphene and Pt/C electrocatalyst was employed as the cathode electrocatalysts of membrane electrode assembly (MEA) at 40 °C without any back pressure. Besides their high open cell voltage (0.99 V) achieved and 3D-Pt@N-Graphene foam showed the maximum current density (Table 2) of 1036.1 $mAcm^{-2}$, respectively, which is remarkably higher than the value of 3D-Pt@ graphene foam (979.1), Pt@N-Graphene (870.2 $mAcm^{-2}$) and Pt/C (644.6 $mAcm^{-2}$). The peak power density of 3D-Pt@N-Graphene foam achieved was 394 $mWcm^{-2}$, which is 1.13, 1.36 and 1.96 times higher than that of 3D-Pt@Graphene foam, Pt@N-Graphene and state-of-the-art Pt/C electrocatalysts. It is demonstrated that the performance is not only related to the presence of porous structure present in the electrocatalyst material. The nitrogen species present in the material also significantly contributed to the enhancement of electrocatalytic performance. Therefore, it can be suggested that both porous structure and nitrogen doping have significant roles on its performance.

View Article Online
DOI: 10.1039/C8SE00552D

Journal Name

ARTICLE

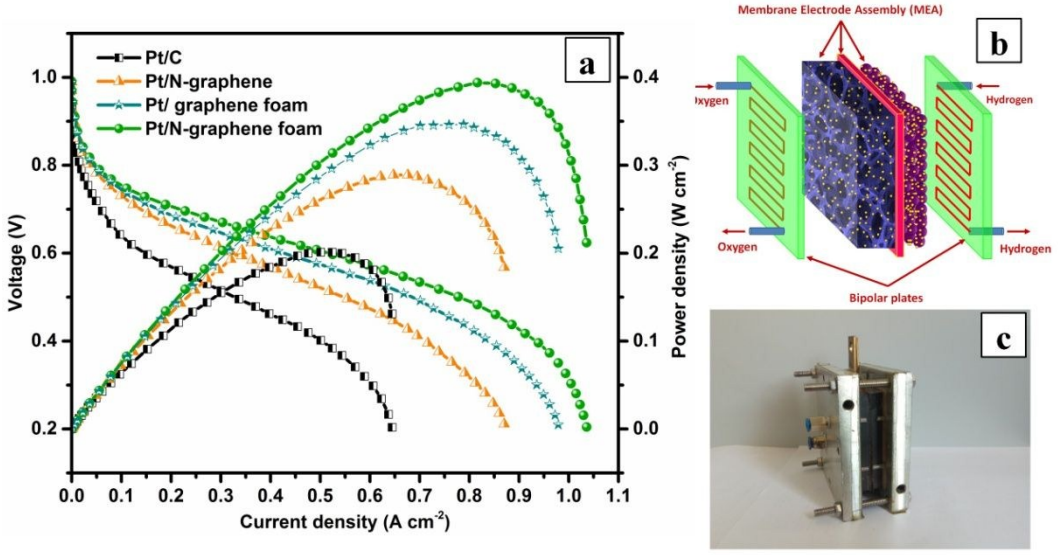

Figure 9. (a) Polarization and power density curves of single PEM fuel cell employed 3D-Pt@N-Graphene foam, 3D-Pt@graphene foam, Pt@N-graphene and Pt/C as a cathode catalyst, (b) schematic illustration of MEA with cell components and (c) assembly of single fuel cell.

Table 2. Fuel cell performance parameters of the different cathode electrocatalysts

Cathode electrocatalyst	OCV (mV)	Current density at P_{max}(mAcm^{-2})	Maximum power density (mWcm^{-2})	Maximum current density (mAcm^{-2})
3D-Pt@N-Graphene foam	991	816.4	394	1036.1
3D-Pt@ Graphene foam	988	788.3	346	979.1
Pt@N-Graphene	989	676.3	289	870.2
Commercial Pt/C	937	523.9	201	644.6

Therefore, the results suggested that 3D-Pt@N-Graphene foam had higher PEMFCs performance as compared to Pt/C is mainly because of the nitrogen doping and 3D foam structure. The favorable electrocatalytic activity and stability of this 3D-Pt@N-Graphene foam cathode for fuel cell can be attributed to several reasons: i) the existence of 2D graphene sheets in the foam network provide high electronic conductivity; ii) the incorporation of nitrogen atom facilitates a homogeneous dispersion of catalyst particles and strengthen the interactions between the catalyst and support; iii) the optimum level of graphitic nitrogen and pyridinic/pyrrolic doping can enhances the electronic conductivity and electrocatalytic activity, respectively; iv) high specific surface area and porous structure in the foam provide smooth fuel diffusion, conductive pathways and adequate ionic contact with the electrolyte. Moreover, the low cost of 3D-Pt@N-Graphene foam fabrication will contribute to the cost reduction of PEM fuel cells, which will expedite their commercialization.

Conclusions

To summarize, porous, flexible hybrid 3D-Pt@N-graphene foam was developed with superior electrocatalytic performance for PEM fuel cell applications. Nitrogen doping of graphene foam was successfully achieved by hydrothermal method with nitrogen doping ratio of 7.17 %. The Pt electrocatalyst nanoparticles were homogeneously integrated with N-doped graphene and their remarkable electrochemical performance of towards ORR was studied under acidic environment which featured the first order kinetics with 4-electron transfer pathway, and possessed high diffusion limiting current density and high positive onset and half wave potential. The Pt@N-graphene foam was found to be highly durable due to strong interactions between the catalyst and support material which prevented agglomeration during cell operation. Single fuel cell testing using Pt@N-graphene foam based MEA yielded 4 times higher current density (1036 mA/cm^2) and maximum power density (394 mW/cm^2) which is much superior to commercial Pt/C electrocatalyst due to the doping of nitrogen in the graphene layers, excellent conductivity, low-resistance

pathways, uniform dispersion and strong interaction of electrocatalyst, high surface area originated from three dimensional porous network and rapid transport of electrolyte ions. The 3D macroporous framework of Pt@N-graphene foam were shortening the diffusion pathways and provided fast mass transfer, while micro/meso porous texture with large surface area enhanced the catalytic active sites and multi-electron transport channels. The improved electrocatalytic properties (triple phase boundaries) of the material revealed its promising applications as an excellent electrocatalyst support material with long-term operational stability of PEM fuel cells.

Conflicts of interest

The authors declare no conflicts of interest.

Acknowledgements

Authors gratefully acknowledge the support of PSG Institute of Advanced Studies, Coimbatore, India, for carrying out this work. The authors also acknowledge DST-SERB (Ref: SB/S3/CE/038/2015) for financial support.

Notes and references

1 H. Lv and S. Mu, *Nanoscale*, 2014, **6**, 5063–5074.
2 A. Brouzgou, S. Q. Song and P. Tsiakaras, *Appl. Catal. B Environ.*, 2012, **127**, 371–388.
3 S. Shahgaldi and J. Hamelin, *Carbon N. Y.*, 2015, **94**, 705–728.
4 L. Dai, Y. Xue, L. Qu, H.-J. Choi and J.-B. Baek, *Chem. Rev.*, 2015, **115**, 4823–4892.
5 J. Stacy, Y. N. Regmi, B. Leonard and M. Fan, *Renew. Sustain. Energy Rev.*, 2017, **69**, 401–414.
6 H. Lv, D. Li, D. Strmcnik, A. P. Paulikas and N. M. Markovic, *Nano Energy*, 2016, **29**, 149–165.
7 N. Jung, D. Y. Chung, J. Ryu, S. J. Yoo and Y. E. Sung, *Nano Today*, 2014, **9**, 433–456.
8 W. Yu, M. D. Porosoff and J. G. Chen, *Chem. Rev.*, 2012, **112**, 5780–5817.
9 Y. Nie, L. Li and Z. Wei, *Chem. Soc. Rev.*, 2015, **44**, 2168–2201.
10 J. Wang, W. Liu, G. Luo, Z. Li, C. Zhao, H. Zhang, M. Zhu, Q. Xu, X. Wang, C. Zhao, Y. Qu, Z. Yang, T. Yao, Y. Li, Y. Lin, Y. Wu and Y. Li, *Energy Environ. Sci.*, 2018, **11**, 3375–3379.
11 B. P. Vinayan, R. Nagar, N. Rajalakshmi and S. Ramaprabhu, *Adv. Funct. Mater.*, 2012, **22**, 3519–3526.
12 S. Guo, S. Zhang and S. Sun, *Angew. Chemie - Int. Ed.*, 2013, **52**, 8526–8544.
13 K. K. Karuppanan, A. V. Raghu, M. K. Panthalingal, S. Ramanathan, T. Kumaresan and B. Pullithadathil, *J. Mater. Chem. A*, 2018, **4**, 10986–10991.
14 G. Bae, D. H. Youn, S. Han and J. S. Lee, *Carbon N. Y.*, 2013, **51**, 274–281.
15 J. Liu, C. T. Liu, L. Zhao, J. J. Zhang, L. M. Zhang and Z. B. Wang, *Int. J. Hydrogen Energy*, 2016, **41**, 1859–1870.
16 H. Huang and X. Wang, *J. Mater. Chem. A*, 2014, **2**, 6266–6291.
17 E. P. Ambrosio, M. A. Dumitrescu, C. Francia, C. Gerbaldi and P. Spinelli, *Fuel Cells*, 2009, **9**, 197–200.
18 Y. Zhou, K. Neyerlin, T. S. Olson, S. Pylypenko, J. Bult, H. N. Dinh, T. Gennett, Z. Shao and R. O'Hayre, *Energy Environ. Sci.*, 2010, **3**, 1437.
19 N. Karthikeyan, B. P. Vinayan, M. Rajesh, K. Balaji, A. K. Subramani and S. Ramaprabhu, *Fuel Cells*, 2015, **15**, 278–287.
20 L. Dubau, L. Castanheira, F. Maillard, M. Chatenet, O. Lottin, G. Maranzana, J. Dillet, A. Lamibrac, J. C. Perrin, E. Moukheiber, A. Elkaddouri, G. De Moor, C. Bas, L. Flandin and N. Caqué, *Wiley Interdiscip. Rev. Energy Environ.*, 2014, **3**, 540–560.
21 J. C. Meier, C. Galeano, I. Katsounaros, A. A. Topalov, A. Kostka, F. Schu and K. J. J. Mayrhofer, *ACS Catal.*, 2012, **2**, 832–843.
22 E. P. Randviir and C. E. Banks, *Electroanalysis*, 2014, **26**, 76–83.
23 B. Y. Xia, Y. Yan, X. Wang and X. W. Lou, *Mater. Horizons*, 2014, **1**, 379–399.
24 A. Ambrosi, C. K. Chua, A. Bonanni and M. Pumera, *Chem. Rev.*, 2014, **114**, 7150–7188.
25 A. V. Raghu, K. K. Karuppanan and B. Pullithadathil, *ACS Sensors*, 2018, acssensors.8b00544.
26 J.-C. Li, P.-X. Hou and C. Liu, *Small*, 2017, **1702002**, 1702002.
27 L. Wang, A. Ambrosi and M. Pumera, *Angew. Chemie - Int. Ed.*, 2013, **52**, 13818–13821.
28 Y. Zheng, Y. Jiao, M. Jaroniec, Y. Jin and S. Z. Qiao, *Small*, 2012, **8**, 3550–3566.
29 L. Sun, L. Wang, C. Tian, T. Tan, Y. Xie, K. Shi, M. Li and H. Fu, *RSC Adv.*, 2012, **2**, 4498.
30 T. Wang, L. Wang, D. Wu, W. Xia, H. Zhao and D. Jia, *J. Mater. Chem. A*, 2014, **2**, 8352–8361.
31 N. Daems, X. Sheng, I. F. J. Vankelecom and P. P. Pescarmona, *J. Mater. Chem. A*, 2014, **2**, 4085–4110.
32 H. Liu, Z. Shi, J. Zhang, L. Zhang and J. Zhang, *J. Mater. Chem.*, 2009, **19**, 468.
33 T. Xing, Y. Zheng, L. H. Li, B. C. C. Cowie, D. Gunzelmann, S. Z. Qiao, S. Huang and Y. Chen, *ACS Nano*, 2014, **8**, 6856–6862.
34 X. Zhou, J. Qiao, L. Yang and J. Zhang, *Adv. Energy Mater.*, 2014, **4**, 1–25.
35 Y. Zhang, J. Ge, L. Wang, D. Wang, F. Ding, X. Tao and W. Chen, *Sci. Rep.*, 2013, **3**, 1–8.
36 G. Neri, A. Scala, F. Barreca, E. Fazio, P. G. Mineo, A. Mazzaglia, G. Grassi and A. Piperno, *Chem. Commun.*, 2015, **51**, 4846–4849.
37 R. Carrera-Cerritos, V. Baglio, A. S. Aricò, J. Ledesma-García, M. F. Sgroi, D. Pullini, A. J. Pruna, D. B. Mataix, R. Fuentes-Ramírez and L. G. Arriaga, *Appl. Catal. B Environ.*, 2014, **144**, 554–560.
38 M. S. Ahmed and Y. B. Kim, *Sci. Rep.*, 2017, **7**, 1–13.
39 A. Nieto, R. Dua, C. Zhang, B. Boesl, S. Ramaswamy and A. Agarwal, *Adv. Funct. Mater.*, 2015, **25**, 3916–3924.
40 B. Shen, Y. Li, W. Zhai and W. Zheng, *ACS Appl. Mater. Interfaces*, 2016, **8**, 8050–8057.
41 K. Lu, J. Xu, J. Zhang, B. Song and H. Ma, *ACS Appl. Mater. Interfaces*, 2016, **8**, 17402–17408.
42 R. Tian, Y. Zhang, Z. Chen, H. Duan, B. Xu, Y. Guo, H. Kang, H. Li and H. Liu, *Sci. Rep.*, 2016, **6**, 1–9.
43 J. K. Wang, G. M. Xiong, M. Zhu, B. Özyilmaz, A. H. Castro Neto, N. S. Tan and C. Choong, *ACS Appl. Mater. Interfaces*, 2015, **7**, 8275–8283.
44 Z. Lu, M. Sun, T. Xu, Y. Li, W. Xu, Z. Chang, Y. Ding, X. Sun and L. Jiang, *Adv. Mater.*, 2015, **27**, 2361–2366.

45 D. . C. Marcano, D. . V Kosynkin, J. M. Berlin, A. Sinitskii, Z. Z. Sun, A. Slesarev, L. B. Alemany, W. Lu and J. M. Tour, *ACS Nano*, 2010, **4**, 4806–4814.
46 S. Stankovich, D. A. Dikin, R. D. Piner, K. A. Kohlhaas, A. Kleinhammes, Y. Jia, Y. Wu, S. B. T. Nguyen and R. S. Ruoff, *Carbon N. Y.*, 2007, **45**, 1558–1565.
47 S. Zhang, Z. Wen, K. Rui, C. Shen, Y. Lu and J. Yang, *J. Mater. Chem. A*, 2015, **3**, 2568–2571.
48 M. J. Fernández-Merino, L. Guardia, J. I. Paredes, S. Villar-Rodil, P. Solís-Fernández, A. Martínez-Alonso and J. M. D. Tascón, *J. Phys. Chem. C*, 2010, **114**, 6426–6432.
49 A. R. O. Raji, T. Varadhachary, K. Nan, T. Wang, J. Lin, Y. Ji, B. Genorio, Y. Zhu, C. Kittrell and J. M. Tour, *ACS Appl. Mater. Interfaces*, 2016, **8**, 3551–3556.
50 D. He, Y. Jiang, H. Lv, M. Pan and S. Mu, *Appl. Catal. B Environ.*, 2013, **132–133**, 379–388.
51 Y. Qin, L. Chao, J. Yuan, Y. Liu, F. Chu, Y. Kong, Y. Tao and M. Liu, *Chem. Commun.*, 2016, **52**, 382–385.
52 N. Seselj, C. Engelbrekt, Y. Ding, H. A. Hjuler, J. Ulstrup and J. Zhang, *Adv. Energy Mater.*, 2018, **8**, 1702609.
53 A. C. Ferrari and D. M. Basko, *Nat. Nanotechnol.*, 2013, **8**, 235–246.
54 Z. Bo, X. Shuai, S. Mao, H. Yang, J. Qian, J. Chen, J. Yan and K. Cen, *Sci. Rep.*, 2014, **4**, 1–8.
55 S. Gao, X. Li, L. Li and X. Wei, *Nano Energy*, 2017, **33**, 334–342.
56 D. Du, P. Li and J. Ouyang, *ACS Appl. Mater. Interfaces*, 2015, **7**, 26952–26958.
57 G. Nam, S. Choi, H. Byun, Y. M. Rhym and S. E. Shim, *Macromol. Res.*, 2013, **21**, 958–964.
58 R. M. Hodlur and M. K. Rabinal, *Compos. Sci. Technol.*, 2014, **90**, 160–165.
59 Y. Xue, J. Liu, H. Chen, R. Wang, D. Li, J. Qu and L. Dai, *Angew. Chemie - Int. Ed.*, 2012, **51**, 12124–12127.
60 P. Kanninen, M. Borghei, O. Sorsa, E. Pohjalainen, E. I. Kauppinen, V. Ruiz and T. Kallio, *Appl. Catal. B Environ.*, 2014, **156–157**, 341–349.
61 Z. Yang, H. Nie, X. Chen, X. Chen and S. Huang, *J. Power Sources*, 2013, **236**, 238–249.
62 L. Qu, Y. Liu, J. Baek and L. D. Ǵ, 2010, **4**, 1321–1326.
63 X. Zhou, S. Tang, Y. Yin, S. Sun and J. Qiao, *Appl. Energy*, 2016, **175**, 459–467.
64 J. Zhang, Z. Zhang and X. Zhao, *RSC Adv.*, 2015, **5**, 104822–104828.
65 K. Gong, F. Du, Z. Xia, M. Durstock and L. Dai, *Science.*, 2009, **323**, 760–764.
66 G. Liu, X. Li, J.-W. Lee and B. N. Popov, *Catal. Sci. Technol.*, 2011, **1**, 207.
67 A. V. Raghu, K. K. Karuppanan and B. Pullithadathil, *Adv. Mater. Interfaces*, 2019, **2**, 1801714.
68 K. K. Karthikeyan and P. Biji, *Microporous Mesoporous Mater.*, 2016, **224**, 372–383.
69 X. Li, B. Y. Guan, S. Gao and X. W. David Lou, *Energy Environ. Sci.*, , DOI:10.1039/C8EE02779J.
70 D. P. He, C. Zeng, C. Xu, N. C. Cheng, H. G. Li, S. C. Mu and M. Pan, *Langmuir*, 2011, **27**, 5582–5588.
71 K. Mohanraju, G. Kousik and L. Cindrella, *New J. Chem.*, 2016, **40**, 8681–8695.
72 H. W. Liang, X. Cao, F. Zhou, C. H. Cui, W. J. Zhang and S. H. Yu, *Adv. Mater.*, 2011, **23**, 1467–1471.
73 O. Antoine, Y. Bultel and R. Durand, *J. Electroanal. Chem.*, 2001, **499**, 85–94.
74 H. Peng, Z. Mo, S. Liao, H. Liang, L. Yang, F. Luo, H. Song, Y. Zhong and B. Zhang, *Sci. Rep.*, 2013, **3**, 1–7.
75 L. Zhang, J. Niu, L. Dai and Z. Xia, *Langmuir*, 2012, **28**, 7542–7550.
76 N. Soin, S. Sinha Roy, S. Roy, K. S. Hazra, D. S. Misra, T. H. Lim, C. J. Hetherington and J. A. McLaughlin, *J. Phys. Chem. C*, 2011, **115**, 5366–5372.
77 B. Zheng, J. Wang, F. Bin Wang and X. H. Xia, *Electrochem. commun.*, 2013, **28**, 24–26.

View Article Online
DOI: 10.1039/C8SE00552D

TABLE OF CONTENTS

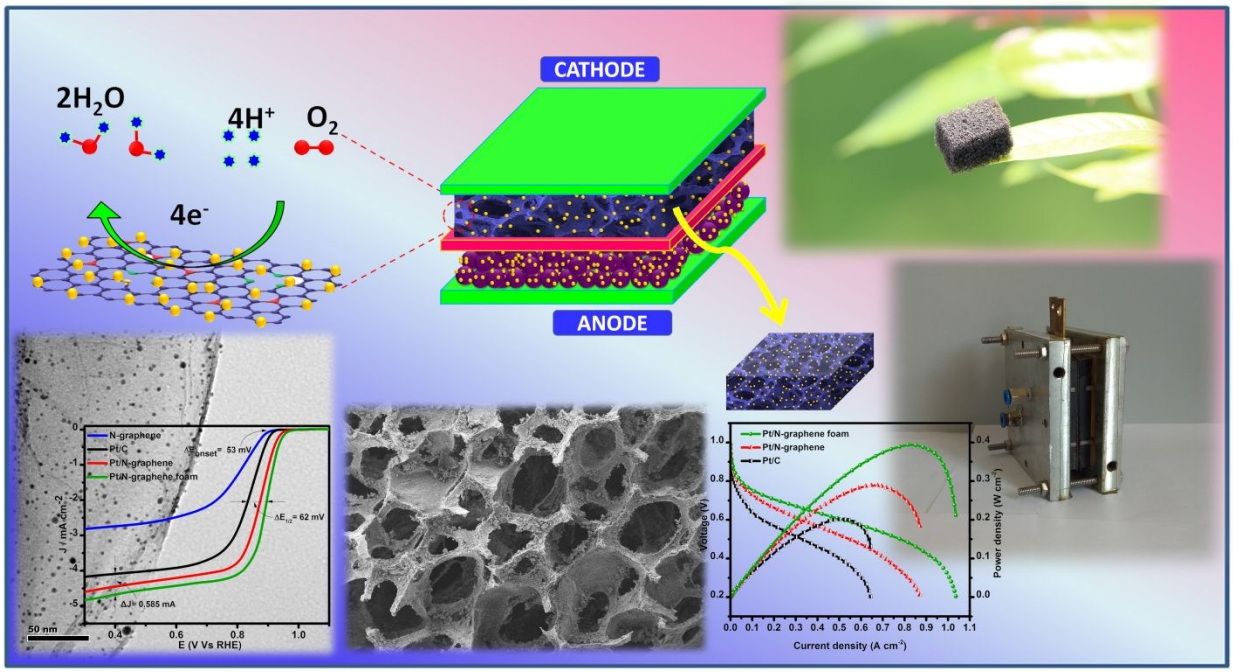

Highlights

- A new class of sustainable electrocatalyst based on Pt@N-Doped Graphene foam is developed for oxygen reduction reaction of PEMFCs.